

The 69th special feature "Frontiers of Molten Salts and Ionic Liquids"

Highly Efficient Water Electrolysis Using NaOH–KOH Hydrate Melt[†]

Keita GOTO,[§] Kenji KAWAGUCHI,^{*,§§} and Toshiyuki NOHIRA^{*,§§§}



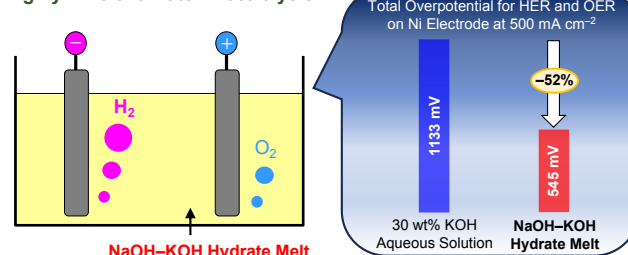
Institute of Advanced Energy, Kyoto University, Gokasho, Uji, Kyoto 611-0011, Japan

* Corresponding authors: kawaguchi.kenji.6a@kyoto-u.ac.jp (K. K.), nohira.toshiyuki.8r@kyoto-u.ac.jp (T. N.)

ABSTRACT

To enhance the efficiency of water electrolysis, this study focuses on the NaOH–KOH hydrate melt (NaOH : KOH : H₂O = 9 : 61 : 30 mol%) at temperatures ranging from 100 to 200 °C. We examined the behaviors of hydrogen and oxygen evolution reactions (HER and OER) on a Ni electrode at atmospheric pressure. In the Tafel plots, the upper limit of the Tafel region for both HER and OER expanded with increasing temperature, especially at 200 °C. Additionally, changes in the rate-determining step for HER and OER were observed compared to a 30 wt% KOH aqueous solution at 80 °C. The total overpotential for HER and OER was compared to the value of 1133 mV obtained in the 30 wt% KOH aqueous solution (80 °C, 500 mA cm⁻²). The total overpotentials in the NaOH–KOH hydrate melt at 200 °C and 500, 1000, and 2000 mA cm⁻² were 545, 619, and 714 mV, respectively. The reduction in overpotentials was 52 %, 45 %, and 37 %, respectively. Water electrolysis utilizing the NaOH–KOH hydrate melt shows promising potential for significantly enhancing energy efficiency even at higher current densities relative to traditional alkaline water electrolysis.

Highly Efficient Water Electrolysis



© The Author(s) 2023. Published by ECSJ. This is an open access article distributed under the terms of the Creative Commons Attribution-NonCommercial-ShareAlike 4.0 License (CC BY-NC-SA, <http://creativecommons.org/licenses/by-nc-sa/4.0/>), which permits non-commercial reuse, distribution, and reproduction in any medium by share-alike, provided the original work is properly cited. For permission for commercial reuse, please email to the corresponding author. [DOI: 10.5796/electrochemistry.23-69153].



Keywords : Water Electrolysis, NaOH–KOH Hydrate Melt, Hydrogen Evolution, Oxygen Evolution

1. Introduction

Recent advancements have positioned hydrogen as a promising secondary energy, particularly in the context of the widespread adoption of renewable energy technologies. Despite their potential, renewable sources like photovoltaic and wind power are subject to variability due to weather and climatic conditions.¹ To address this challenge, the “Hydrogen Energy System”² has been proposed as an effective solution for managing the intermittency of renewable energy sources. This system involves converting electricity derived from renewable sources into hydrogen or other hydrogen-based carriers, such as ammonia or organic hydrides, for efficient large-scale energy storage and transportation. Subsequently, the stored energy is reconverted into electricity using fuel cells or hydrogen turbines.³

Water electrolysis is a critical component of the hydrogen energy system and is instrumental in hydrogen production. This process is environmentally friendly, producing hydrogen without emitting greenhouse gases or other pollutants. However, producing hydrogen via water electrolysis, particularly when powered by renewable

energy, is more expensive than conventional fossil fuel-based methods and has not yet seen widespread commercial adoption.^{4,5} In 2022, a mere 0.1 % of global hydrogen production was attributed to water electrolysis, while over 80 % was produced from fossil fuels.⁶ A significant factor contributing to the high cost of hydrogen production via electrolysis is its low energy efficiency, stemming from substantial overpotentials in hydrogen evolution reaction (HER) and oxygen evolution reaction (OER), as well as ohmic losses.

Alkaline water electrolysis (AWE) currently stands as one of the predominant commercial methods for water electrolysis.^{4,7–10} In commercial settings, AWE typically employs an electrolyte comprising 20–40 wt% KOH aqueous solution and operates at temperatures ranging from 70 to 90 °C, under pressures below 30 atm.⁷ Nonetheless, conducting AWE at higher temperatures is anticipated to yield numerous advantages.¹¹ Elevated temperature operation of AWE can lead to several benefits, including a reduction in the theoretical decomposition voltage due to thermodynamic effects, decreased overpotentials of HER and OER owing to kinetic effects, and diminished ohmic loss in the electrolyte.

Despite these anticipated advantages, there are limited studies on AWE at temperatures exceeding 150 °C.^{12–19} For example, Miles et al. investigated the temperature dependency of HER and OER behaviors in the range of 80–264 °C using a 50 wt% KOH aqueous solution.¹² In their study, the internal pressure of the cell was regulated to a maximum of 15 atm to prevent electrolyte evaporation. Similarly, Ganley examined HER and OER behaviors at temperatures from 35 to 400 °C under pressures between 1 and 86 atm in a 52 wt% KOH aqueous solution.¹³ Other high-temper-

[†] A part of this paper has been presented in 2023 Joint Symposium on Molten Salts (Presentation #P59).

[§]ECSJ Student Member

^{§§}ECSJ Active Member

^{§§§}ECSJ Fellow

K. Kawaguchi orcid.org/0000-0002-8883-9040

T. Nohira orcid.org/0000-0002-4053-554X

ature AWE studies have also necessitated additional pressure to maintain prevent electrolyte evaporation.^{14–19} To our knowledge, the highest temperature AWE conducted under atmospheric pressure in an alkaline aqueous solution was reported by Wendt and Plzak, who achieved a temperature of 130 °C using a 50 wt% KOH aqueous solution.²⁰ Since the boiling point of a 50 wt% KOH aqueous solution is 145 °C,²¹ conducting water electrolysis at 150 °C or higher under atmospheric pressure is unfeasible within an aqueous solution system. If not limited to aqueous solution systems, Divisek et al. have reported water electrolysis at temperatures between 300 and 400 °C under atmospheric pressure using a molten NaOH or a molten NaOH–LiOH mixture, by introducing water vapor into the electrolyte.^{22,23}

In pursuit of enhancing the energy efficiency of water electrolysis by operating at temperatures higher than conventional methods, our study explores the use of hydrate melt electrolytes, characterized by significantly lower water content compared to traditional aqueous solutions. Our previous research demonstrated that water electrolysis in an 85 wt% KOH hydrate melt (KOH : H₂O = 65 : 35 mol%) at 150 °C under atmospheric pressure substantially reduced the overpotentials of HER and OER at a Ni electrode, in comparison to a standard 30 wt% KOH aqueous solution (KOH : H₂O = 12 : 88 mol%) at 80 °C.²⁴ Nevertheless, the high melting point of the 85 wt% KOH hydrate melt (= 100.4 °C²⁵) poses potential operational challenges in practical electrolyzer applications.

This study focuses on water electrolysis using NaOH–KOH hydrate melt. Initially, we measured melting points of NaOH–KOH hydrate melts with various compositions to identify a lower melting point for the electrolyte. We then assessed the potential stability of a palladium hydride (Pd–H) electrode, employed as the reference electrode, in the NaOH–KOH hydrate melt. Finally, the behaviors of HER and OER on a Ni electrode in the NaOH–KOH hydrate melt, within the temperature range of 100–200 °C under atmospheric pressure, were investigated using linear sweep voltammetry (LSV). The results were then compared with those obtained in the 30 wt% KOH aqueous solution at 80 °C and in KOH hydrate melt at 150 °C.

2. Experimental

2.1 Melting point measurement of NaOH–KOH hydrate melt

Melting points of NaOH–KOH hydrate melts were measured for a variety of compositions. The NaOH–KOH hydrate melts were prepared using NaOH and KOH sourced from FUJIFILM Wako Pure Chemical Corp., both designated as Guaranteed Reagent. The purity of these reagents, determined by neutralization titration, was 98.5 ± 0.3 % for NaOH and 86.3 ± 0.3 % for KOH. This was achieved by completely melting the hydrate melt with heating, followed by gradual cooling under stirring. The temperature at which the colorless liquid began to turn cloudy was identified as the melting point. For comparative purposes, the melting point of an 85 wt% KOH hydrate melt was also measured under an Ar gas flow at atmospheric pressure.

2.2 Electrochemical measurements

According to the melting point measurement, the optimal composition of the NaOH–KOH hydrate melt was determined as NaOH : KOH : H₂O = 9 : 61 : 30 mol% (equivalent to 8 : 79 : 13 wt%), which was used for electrochemical measurements. Electrochemical measurements were conducted in a three-electrode cell configuration using an electrochemical measurement system (Hokuto Denko Corp., HZ-7000). Figure 1 illustrates a schematic of this three-electrode cell. The cell comprised a perfluoroalkyl alkanes (PFA) beaker, a polytetrafluoroethylene (PTFE) cover, and various electrodes. The electrolytes employed included 500 g of either NaOH–KOH hydrate melt, 30 wt% KOH aqueous solution, or 85 wt% KOH hydrate melt. A flag-shaped Ni plate (99.95 % purity,

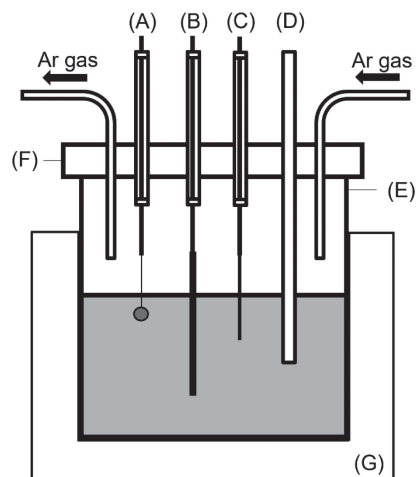


Figure 1. A schematic drawing of the experimental apparatus; (A) working electrode, (B) counter electrode, (C) reference electrode, (D) PTFE coated thermocouple, (E) PFA beaker, (F) PTFE cover, and (G) mantle heater.

Table 1. Equilibrium potentials of (a) $\text{H}_2\text{O} + \text{e}^- \rightleftharpoons \text{H}(\text{Pd}) + \text{OH}^-$ and (b) $2 \text{OH}^- \rightleftharpoons 1/2 \text{O}_2 + \text{H}_2\text{O} + 2\text{e}^-$ vs. RHE at each temperature.

Temperature/°C	Potential vs. RHE/mV	
	(a) H ₂ O/H(Pd)	(b) OH ⁻ /O ₂
80	36	1183
100	26	1167
120	15	1162
150	0	1155
180	-15	1147
200	-24	1142

sourced from Nilaco Corp., with a diameter of 3.0 mm, thickness of 0.1 mm, and a surface area of 0.157 cm² included Ni lead wire) served as the working electrode.²⁶ The counter electrode was either a Ni rod (99.0 % purity, Nilaco Corp., diameter: 1.5 mm) or a Pt rod (99.95 % purity, TANAKA Kikinzoku Kogyo K.K., diameter: 2.0 mm). A Pd–H electrode was used as the reference electrode in the NaOH–KOH and KOH hydrate melts, while a reversible hydrogen electrode (RHE) was utilized in the 30 wt% KOH aqueous solution. Before the electrochemical measurements, a preliminary electrolysis was conducted with a Pt rod anode and a Ni rod cathode at 100 mA cm⁻² (129 mA) for 20 h.

LSV was carried out at 10 mV s⁻¹ in the NaOH–KOH hydrate melt at temperatures of 100, 120, 150, 180, and 200 °C, in 30 wt% KOH aqueous solution at 80 °C, and in 85 wt% KOH hydrate melt at 150 °C. The potential of Pd–H electrode was calibrated relative to the RHE. The equilibrium potential for the Pd–H electrode with respect to the RHE was established through thermodynamic calculations, considering the constant hydrogen activity and the temperature in the two-phase coexistence region of Pd–H.^{27,28} Table 1 shows the equilibrium potential of the Pd–H electrode relative to RHE at each temperature. The equilibrium potential of OER vs. RHE at each temperature is also shown in Table 1. Thermodynamic calculations for these equilibrium potentials are detailed in the Supporting Information.

All measured potentials were in-situ IR-compensated by the positive feedback method (feedback rate: 95 %) using the resistance value measured by the AC impedance method.

The Pd–H electrode was fabricated by galvanostatic electrolysis of a Pd wire (99.9% purity, Nilaco Corp., diameter: 1.0 mm) at -10 mA cm^{-2} over 20 h. To verify the potential stability of the Pd–H electrode, its potential was measured intermittently using a dynamic hydrogen electrode (DHE) in the NaOH–KOH hydrate melt at 150°C . The DHE was prepared, employing galvanostatic electrolysis on a flag-shaped Pt plate (99.95% purity, Nilaco Corp., diameter: 3.0 mm, thickness: 0.1 mm, surface area: 0.157 cm^2) at -10 mA cm^{-2} .

All electrochemical measurements were conducted in stationary electrolytes under Ar gas flow at atmospheric pressure. Under the present experimental conditions (maximum duration of experiment 48 h, temperature range $100\text{--}200^\circ\text{C}$, Ar gas flow rate $20\text{--}50 \text{ mL min}^{-1}$), there was virtually no evaporation of the electrolyte. In addition, the composition of the NaOH–KOH hydrate melt was not substantially changed by water consumption due to electrolysis, as an ample quantity of electrolyte was employed.

3. Results and Discussion

3.1 Melting point measurement of NaOH–KOH hydrate melt

Table 2 presents the melting points of various NaOH–KOH hydrate melt compositions. Figure 2 graphically represents these compositions, specifically entries 1–7 from Table 2, on a ternary diagram, including the reported eutectic composition.²⁹ The melting point for the composition in entry 1 (KOH : H₂O = 65 : 35 mol% = 85 : 15 wt%) of the KOH hydrate melt, used as a reference, was determined to be 101°C . This value closely aligns with the previously reported melting point of 100.4°C .²⁵

Table 2. Measured melting points of NaOH–KOH hydrate melts at various compositions and the reported eutectic point.

Entry	NaOH : KOH : H ₂ O		Melting point / $^\circ\text{C}$
	/ mol%	/ wt%	
1	0 : 65 : 35	0 : 85 : 15	101
2	9 : 61 : 30	8 : 79 : 13	88
3	7 : 62 : 31	6 : 81 : 13	88
4	11 : 59 : 30	10 : 77 : 13	90
5	8 : 56 : 36	8 : 76 : 16	120
6	31 : 31 : 37	34 : 48 : 18	150
7	26 : 26 : 48	31 : 43 : 26	103
Eutectic ²⁹	9 : 62 : 29	8 : 80 : 12	90

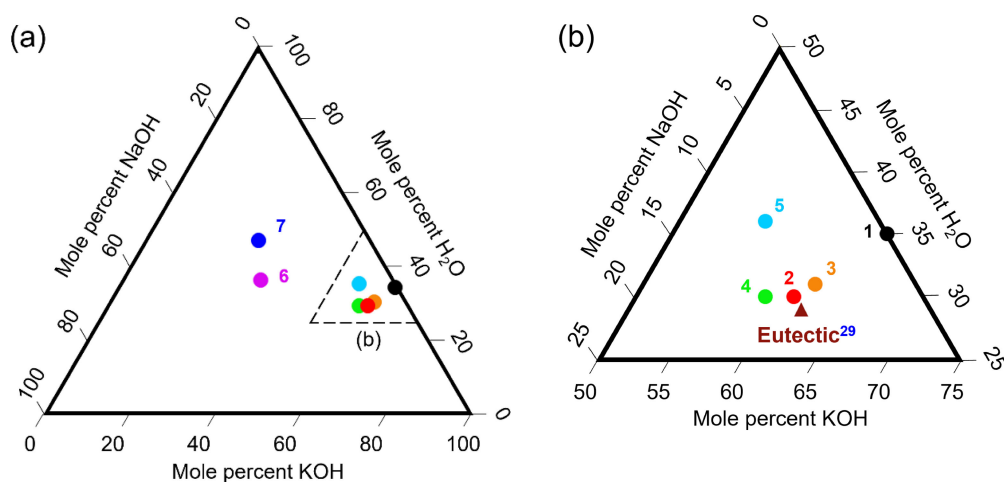


Figure 2. Compositions of Entry 1–7 for melting points measurement and the eutectic composition from the literature.²⁹ (a) The full scale of ternary diagram and (b) the area enclosed by broken lines in (a).

For the NaOH–KOH hydrate melt, the initial measurement focused on entry 2 (NaOH : KOH : H₂O = 9 : 61 : 30 mol% = 8 : 79 : 13 wt%), closely matching the reported eutectic composition²⁹ (NaOH : KOH : H₂O = 9 : 62 : 29 mol% = 8 : 80 : 12 wt%). The measured melting point of 88°C for entry 2 is slightly lower than the reported eutectic point of 90°C ²⁹ and 13°C lower than that of the KOH hydrate melt in entry 1. It is important to note that the available NaOH and KOH pellets did not permit the preparation of a NaOH–KOH hydrate melt with the exact reported eutectic composition due to excessive total water content.

For entries 3 and 4, which have slightly less and more NaOH than entry 2, respectively, the melting points were recorded as 88°C and 90°C . Entry 5, with a higher water content than entry 2, exhibited a substantial increase in melting point to 120°C .

Considering that the eutectic composition of the binary NaOH–KOH system is approximately equimolar,³⁰ we expected low melting points with NaOH : KOH ratios of 1 : 1 but varying water contents (entries 6 and 7). However, the melting point of entry 6 (NaOH : KOH : H₂O = 31 : 31 : 37 mol%) was as high as 150°C . In the case of entry 7 (NaOH : KOH : H₂O = 26 : 26 : 48 mol%), though the melting point was 103°C , bubble formation was observed around 140°C as the temperature increased, suggesting that approximately 140°C could be the boiling point. It should be noted that for entries 2–6, no bubble formation was observed even when the temperature was elevated to 200°C .

Consequently, the composition of entry 2, exhibiting the lowest melting point and closest alignment to the reported eutectic composition, was selected as the NaOH–KOH hydrate melt electrolyte for use in this study.

3.2 Potential stability of Pd–H reference electrode

Figure 3 illustrates the potential behavior of the Pd–H electrode in the NaOH–KOH hydrate melt (composition: NaOH : KOH : H₂O = 9 : 61 : 30 mol% = 8 : 79 : 13 wt%) at 150°C over a period of approximately 200 h after the hydride formation. Initially, the potential of Pd–H electrode shifted positively relative to the DHE potential, stabilizing after about 20 h. From 20 to approximately 200 h, the Pd–H electrode maintained a stable potential of $97 \pm 3 \text{ mV}$ vs. DHE. This observed potential shift in the Pd–H electrode can be thermodynamically interpreted:²⁷ the potential variation up to 20 h is attributed to changes in hydrogen activity in Pd–H in the single β -phase composition of Pd–H. After 20 h, the stability of potential is attributed to the constant hydrogen activity in the coexistent $\alpha + \beta$ phase.

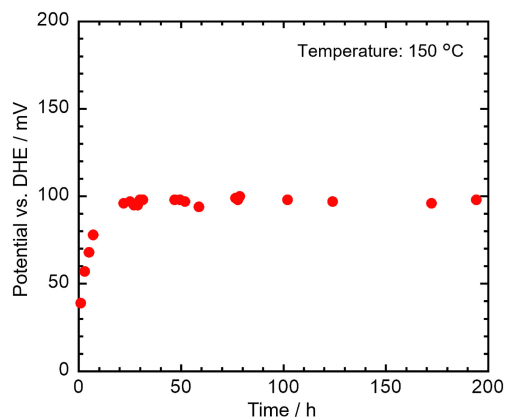


Figure 3. Stability test of a Pd-H reference electrode in the NaOH-KOH hydrate melt at 150 °C. Pd-H electrode was prepared by galvanostatic electrolysis on a Pd electrode at -10 mA cm^{-2} for 20 h. DHE was prepared by galvanostatic electrolysis on a Pt electrode at -10 mA cm^{-2} .

Consequently, the Pd-H electrode, exhibiting the stable potential beyond 20 h post-hydride formation, was employed as the reference electrode in this study.

3.3 HER behaviors on Ni electrode

Figure 4a presents LSVs for HER on a Ni electrode in the NaOH-KOH hydrate melt at various temperatures (100, 120, 150, 180, and 200 °C). Notably, as the temperature of the hydrate melt increased from 100 to 180 °C, there was a distinct positive shift in the onset potential for HER, accompanied by a significant reduction in polarization at higher current densities. At 200 °C, the onset potential closely resembled that at 180 °C, yet with further decreased polarization at high current densities.

Figure 4b displays Tafel plots derived from the LSVs. As the temperature increases from 100 to 180 °C, the upper limit of the Tafel region extends from 50 to 100 mA cm^{-2} . At 200 °C, it further extends to 250 mA cm^{-2} , suggesting enhanced mass transfer for HER with increasing temperature.

For comparison, Fig. 4 also shows the results for the 30 wt% KOH aqueous solution at 80 °C. In the KOH aqueous solution, the onset potential is more negative than that in the NaOH-KOH hydrate melt at 100 °C, whereas the polarization is lower in the high current density region. The upper limit of the Tafel region in the KOH aqueous solution is 250 mA cm^{-2} . These results suggest that mass transfer for HER is suppressed in the NaOH-KOH hydrate melt at 100 to 180 °C compared to that in the KOH aqueous solution at 80 °C.

For comparison of the polarization curve for HER in KOH aqueous solution, two reported results^{20,31} are also plotted in Fig. 4. In Ref. 20, Wendt et al. investigated HER on a sand-blasted Ni electrode in a 50 wt% KOH solution at 70 °C. In Ref. 31, Santos et al. reported the results on an electrodeposited Ni electrode in a 28 wt% KOH solution at 70 °C. Compared to the present results in the 30 wt% KOH aqueous solution at 80 °C, the results of Ref. 20 show a significantly smaller polarization. This is explained by the fact that Ref. 20 used the Ni electrode activated by sand-blasting. On the other hand, the results of Ref. 31 exhibit a larger polarization than those of the present study. One possible reason for this difference is that the electrodeposited Ni used in Ref. 31 had a different surface condition than that of the commercial Ni plate used in the present study.

Figure 5 shows the temperature-dependent Tafel slopes for the HER on a Ni electrode. In the KOH aqueous solution, the Tafel slope is 96 mV dec^{-1} . When utilizing the NaOH-KOH hydrate melt as the electrolyte, a notable decrease in Tafel slope is observed.

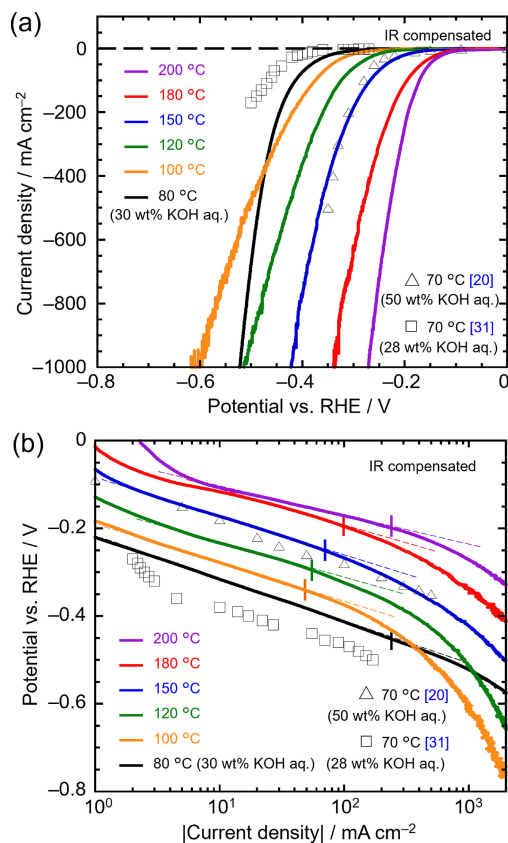


Figure 4. (a) Linear sweep voltammograms and (b) Tafel plots for HER on a Ni electrode in the NaOH-KOH hydrate melt at 100, 120, 150, 180, and 200 °C, and in 30 wt% KOH aqueous solution at 80 °C. Scan rate: 10 mV s^{-1} . The data from literature are also plotted for references; a sand-blasted Ni electrode in 50 wt% KOH aqueous solution at 70 °C²⁰ and an electrodeposited Ni electrode in 28 wt% KOH aqueous solution at 70 °C.³¹

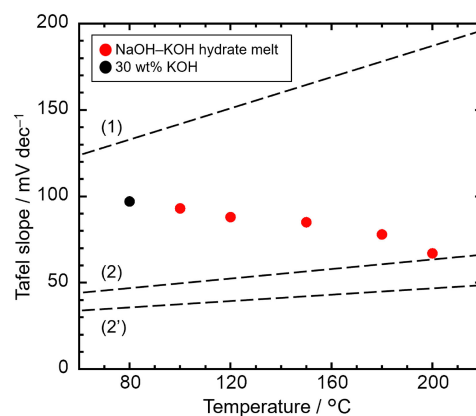
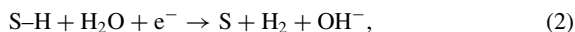


Figure 5. Temperature dependence of Tafel slope for HER on a Ni electrode in the NaOH-KOH hydrate melt at 100–200 °C. Tafel slope on a Ni electrode in 30 wt% KOH aqueous solution at 80 °C is also plotted for reference. Broken lines represent theoretical Tafel slopes when the rate-determining step is step (1), (2), and (2'), respectively.

Specifically, at 200 °C, the Tafel slope exhibits markedly lower value, 67 mV dec^{-1} .

To interpret the mechanism of HER based on Tafel slope analysis, the most widely accepted mechanism in alkaline aqueous solutions involves the following sequence.^{32–34}



where S denotes an active site for HER. The mechanism comprises two primary steps, with the second step proceeding through either an electrochemical route (step 2) or a chemical route (step 2'). In Fig. 5, the broken lines represent theoretical Tafel slopes corresponding to scenarios where step 1, step 2, or step 2' is the rate-determining step. The theoretical Tafel slope for an electrode reaction involving several elementary reactions is derived from the following equation:³⁵

$$\text{Tafel slope} = 2.303 \frac{RT}{(n_b + \beta n_{\text{rds}})F}, \quad (3)$$

where R represents the universal gas constant ($8.314 \text{ J K}^{-1} \text{ mol}^{-1}$), T denotes temperature, F denotes the Faraday constant ($9.6485 \times 10^4 \text{ C mol}^{-1}$), n_b denotes the number of electrons transferred before the rate-determining step, n_{rds} represents the number of electrons transferred during the rate-determining step, and β denotes the symmetry factor, assumed to be 0.5. At 80°C in the KOH aqueous solution, the mixed control of steps 1 and 2 is suggested as the rate-determining steps. In the NaOH–KOH hydrate melt, as the temperature increases from 100 to 180°C , the contribution of step 2 to the mixed control gradually increases. The observed Tafel slope at 200°C closely aligns with theoretical values when step 2 is considered as the rate-determining step.

3.4 OER behaviors on Ni electrode

Figure 6a presents LSVs for the OER on a Ni electrode in the NaOH–KOH hydrate melt across a temperature range of 100 to 200°C . A notable trend is observed where, as the temperature of the hydrate melt increases, the onset potential for OER shifts more negatively, accompanied by a significant reduction in polarization at higher current densities.

Figure 6b displays Tafel plots derived from these LSVs. At the lowest temperature of 100°C , the upper limit of the Tafel region is approximately 20 mA cm^{-2} . As the temperature increases, this limit expands to approximately 250 mA cm^{-2} at 200°C . These observations suggest that mass transfer for OER is significantly enhanced at high temperatures, especially at 200°C .

For comparison, Fig. 6 also shows the results for the 30 wt% KOH aqueous solution at 80°C . The upper limit of the Tafel region in the KOH aqueous solution is 8 mA cm^{-2} . The trend of mass transfer for OER is different from that for HER, suggesting that mass transfer for OER is enhanced in the NaOH–KOH hydrate melt, especially at 150 to 200°C , compared to the KOH aqueous solution at 80°C .

For comparison of the polarization curve for OER in KOH aqueous solution, two reported results^{20,31} are also plotted in Fig. 6. Similar to the case of HER, they were obtained on the sand-blasted Ni electrode in the 50 wt% KOH solution at 70°C ²⁰ and the electrodeposited Ni electrode in the 28 wt% KOH solution at 70°C .³¹ The results of Ref. 20 show a considerably smaller polarization than the present results in the 30 wt% KOH aqueous solution at 80°C . This can be attributed to the used of mechanically activated sand-blasted Ni electrode, as in the case of HER in Section 3.3. For Ref. 31, the results exhibit a smaller polarization compared to the present study. This suggests that the electrodeposited Ni shows a higher activity than the commercial Ni plate with respect to OER. However, a detailed discussion is difficult because surface analysis has not been performed in either the literature^{20,31} or the present study. Reviewing the reports^{20,31,36–41} on the polarization behaviors for OER on Ni-based electrodes in KOH aqueous solutions, the electrode preparation method, shape, surface morphology, chemical state, and the presence of impurities have a significant effect on the polarization behavior.

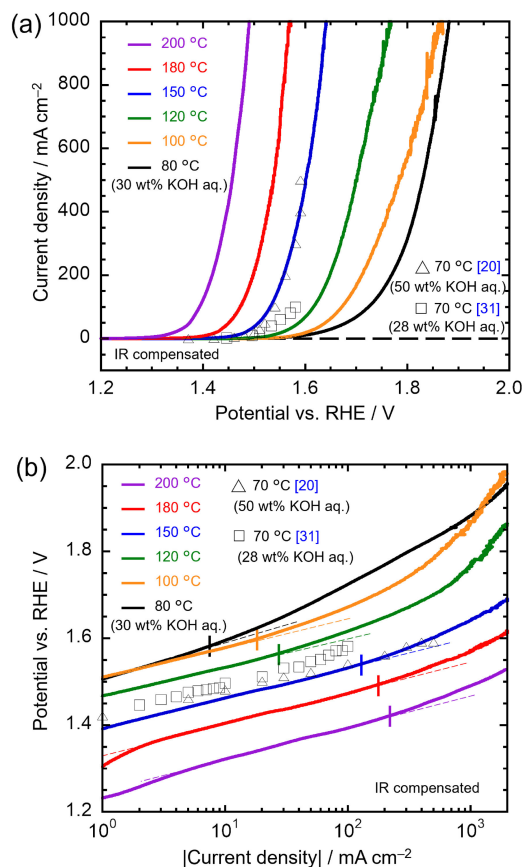


Figure 6. (a) Linear sweep voltammograms and (b) Tafel plots for OER on a Ni electrode in the NaOH–KOH hydrate melt at 100, 120, 150, 180, and 200°C , and in 30 wt% KOH aqueous solution at 80°C . Scan rate: 10 mV s^{-1} . The data from literature are also plotted for references; a sand-blasted Ni electrode in 50 wt% KOH aqueous solution at 70°C ²⁰ and an electrodeposited Ni electrode in 28 wt% KOH aqueous solution at 70°C .³¹

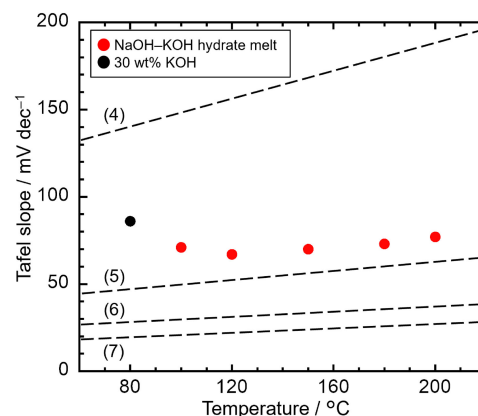
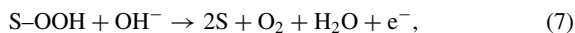
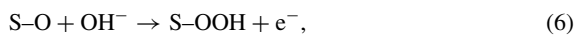
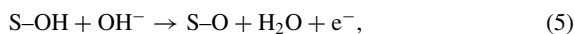


Figure 7. Temperature dependence of Tafel slope for OER on a Ni electrode in the NaOH–KOH hydrate melt at 100 – 200°C . Tafel slope on a Ni electrode in 30 wt% KOH aqueous solution at 80°C is also plotted for reference. Broken lines represent theoretical Tafel slopes when the rate-determining step is step (4), (5), (6), and (7), respectively.

Figure 7 illustrates the temperature-dependent Tafel slopes for OER on a Ni electrode. In the KOH aqueous solution, the Tafel slope for OER is 87 mV dec^{-1} . However, in the NaOH–KOH hydrate melt, there is a decrease in Tafel slopes across the

temperature range: 71 mV dec⁻¹ at 100 °C, 67 mV dec⁻¹ at 120 °C, 70 mV dec⁻¹ at 150 °C, 73 mV dec⁻¹ at 180 °C, and 77 mV dec⁻¹ at 200 °C.

To understand the mechanism of OER, various mechanisms have been proposed depending on the experimental conditions.^{34,36} Among these, the following steps are widely recognized for OER in alkaline aqueous solutions:^{42,43}



where S represents an active site for OER, and the mechanism involves four steps, each comprising a one-electron reaction. The broken lines in Fig. 7 depict theoretical Tafel slopes calculated using Eq. 3, corresponding to scenarios where step 4, 5, 6, or 7 is the rate-determining step. At 80 °C in the KOH aqueous solution, a combination of steps 4 and 5 is suggested as the rate-determining steps. In the NaOH-KOH hydrate melt, the contribution of step 5 to the mixed control appears to be dominant across the temperature range of 100–200 °C, aligning closely with theoretical Tafel slope values when step 5 is considered as the rate-determining step.

3.5 Temperature dependence of overpotentials for HER and OER and comparison with KOH aqueous solution

Figure 8 depicts the temperature dependences of overpotentials for (a) HER and (b) OER at ± 500 , ± 1000 and ± 2000 mA cm⁻² in the NaOH-KOH hydrate melt. The plotted values are based on the LSVs depicted in Figs. 4 and 6. The current density of

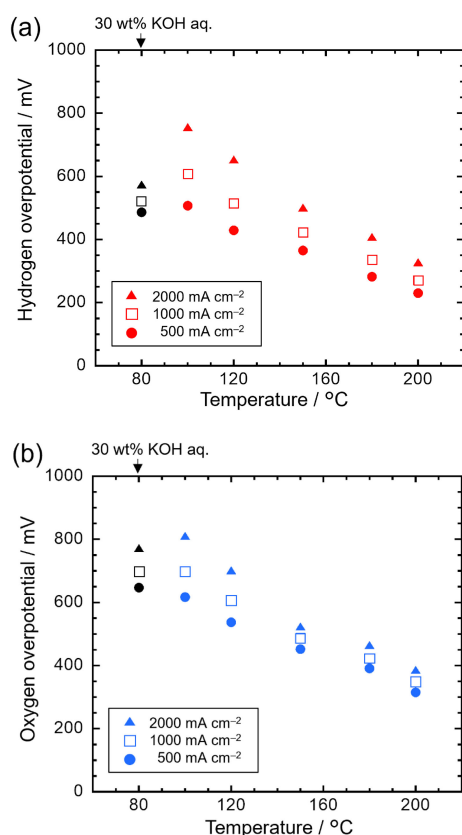


Figure 8. Temperature dependence of (a) HER overpotential and (b) OER overpotential obtained from LSV on a Ni electrode in the NaOH-KOH hydrate melt at 100–200 °C. Overpotentials on a Ni electrode in 30 wt% KOH aqueous solution at 80 °C are also plotted for references. Current density: ± 500 , ± 1000 and ± 2000 mA cm⁻².

± 500 mA cm⁻², corresponds to higher current densities in conventional AWE, while the current densities of ± 1000 and ± 2000 mA cm⁻² are practically impossible for commercial AWE.¹⁰ For comparison, overpotentials for HER and OER in the 30 wt% KOH aqueous solution at 80 °C are also plotted.

In the NaOH-KOH hydrate melt, overpotentials decrease at temperatures above 150 °C for HER and above 120 °C for OER, at all current densities, when compared to the KOH aqueous solution at 80 °C. Notably, the impact of overpotential reduction becomes more pronounced at higher current densities, with a more substantial effect observed for OER compared to HER. Another observation is that the overpotentials for OER consistently exceed those for HER across all temperatures and current densities.

The present overpotentials in the NaOH-KOH hydrate melt at 150 °C are compared with those obtained in the previous reported KOH hydrate melt at the same temperature (Fig. S1). This comparison revealed that the overpotentials for HER were similar in both melts. However, for OER, the overpotentials at 500, 1000, and 2000 mA cm⁻² were found to be 31, 31, and 43 mV lower, respectively, in the NaOH-KOH hydrate melt compared to the KOH hydrate melt. This highlights superior efficacy of the NaOH-KOH hydrate melt in reducing overpotentials, particularly for OER, under high-current-density conditions.

Figure 9 provides a comprehensive summary of the overpotentials for HER and OER at 200 °C in the NaOH-KOH hydrate melt, as shown in Fig. 8. This summary includes data for each current density, highlighting the total overpotential and the corresponding reduction in comparison to the KOH aqueous solution at 500 mA cm⁻² and 80 °C (Total 1133 mV = HER 486 mV + OER 647 mV).

At a current density of 500 mA cm⁻², the total overpotential 545 mV (= HER 230 mV + OER 315 mV) is lower by 588 mV (52 %) compared to the KOH aqueous solution at 80 °C. The standard theoretical decomposition voltage decreased by 41 mV when the temperature increases from 80 °C to 200 °C. Therefore, the combined reduction in overpotential and standard theoretical decomposition voltage totaled 629 mV. This indicates that the decrease in polarization was predominantly due to kinetic effects (93 %), with thermodynamic effects contributing 7 %. At increased current densities of 1000 mA cm⁻², the total overpotential 619 mV (= HER 271 mV + OER 348 mV) is lower by 514 mV (45 %) compared to the KOH aqueous solution at 80 °C. Even at 2000 mA cm⁻², the total overpotential 714 mV (= HER 328 mV +

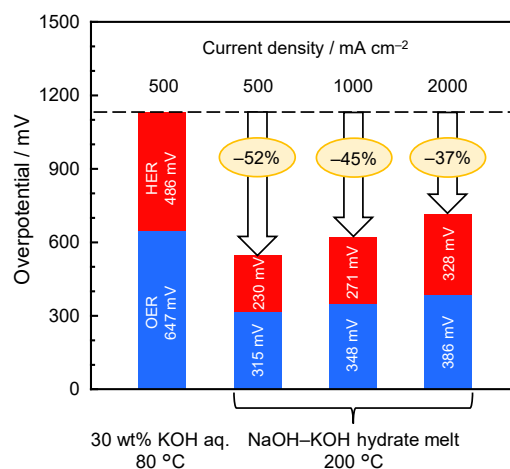


Figure 9. Comparison of overpotential on a Ni electrode in 30 wt% KOH aqueous solution at 80 °C and the NaOH-KOH hydrate melt at 200 °C. Current density: 500 mA cm⁻² in 30 wt% KOH aqueous solution and 500, 1000, and 2000 mA cm⁻² in the NaOH-KOH hydrate melt.

OER 386 mV) is lower by 419 mV (37%) than the KOH aqueous solution at 80 °C.

These findings underscore the potential of water electrolysis using the NaOH–KOH hydrate melt to enhance energy efficiency, even when operated at higher current densities than traditional AWE. Since the overpotentials for HER and OER were evaluated using the three-electrode cell in this study, future studies should include evaluation of the effect of ionic conductivity of NaOH–KOH hydrate melt using a cell with a diaphragm, assuming an actual electrolyzer.

4. Conclusions

In this study, we focused on enhancing water electrolysis efficiency through the use of a NaOH–KOH hydrate melt electrolyte. The optimal composition, NaOH : KOH : H₂O = 9 : 61 : 30 mol% (equivalent to 8 : 79 : 13 wt%), was identified for its low melting point of 88 °C, which is 13 °C below the eutectic point of the conventional KOH hydrate melt (KOH : H₂O = 65 : 35 mol% = 85 : 15 wt%). The potential of the Pd–H electrode was observed to stabilize at 97 ± 3 mV versus the DHE at 150 °C from 20 h to approximately 200 h following hydride formation. We investigated HER and OER behaviors on a Ni electrode in the NaOH–KOH hydrate melt over a temperature range of 100–200 °C under atmospheric pressure. LSV revealed that as the temperature increased, significant decreases in polarization for both HER and OER were observed. In the Tafel plots, the upper limit of the Tafel region for both HER and OER expanded with increasing temperature, especially at 200 °C. Changes in the rate-determining steps for HER and OER were observed when compared to the 30 wt% KOH aqueous solution at 80 °C. The total overpotential for HER and OER was compared to the value of 1133 mV obtained in the 30 wt% KOH aqueous solution (80 °C, 500 mA cm⁻²). The total overpotentials in the NaOH–KOH hydrate melt at 200 °C and 500, 1000, and 2000 mA cm⁻² were 545, 619, and 714 mV, respectively. The reduction in overpotentials was 52 %, 45 %, and 37 %, respectively. Thus, our findings demonstrate the potential of the NaOH–KOH hydrate melt in significantly improving the energy efficiency of water electrolysis, especially at higher operational temperatures.

Acknowledgments

A part of this study was supported by Adaptable and Seamless Technology transfer Program through Target-driven R&D (A-STEP) from Japan Science and Technology Agency (JST) Grant Number JPMJTR23TB.

CRedit Authorship Contribution Statement

Keita Goto: Data curation (Equal), Investigation (Lead), Methodology (Equal), Validation (Equal), Writing – original draft (Lead)
 Kenji Kawaguchi: Conceptualization (Equal), Data curation (Lead), Investigation (Equal), Methodology (Lead), Supervision (Equal), Validation (Equal), Writing – review & editing (Lead)
 Toshiyuki Nohira: Conceptualization (Equal), Funding acquisition (Lead), Methodology (Equal), Project administration (Lead), Supervision (Equal), Validation (Equal), Writing – review & editing (Equal)

Data Availability Statement

The data that support the findings of this study are openly available under the terms of the designated Creative Commons License in J-STAGE Data listed in D1 of References.

Conflict of Interest

The authors declare no conflict of interest in the manuscript.

Funding

Japan Science and Technology Agency: JPMJTR23TB

References

- D1. K. Goto, K. Kawaguchi, and T. Nohira, *J-STAGE Data*, <https://doi.org/10.50892/data.electrochemistry.25294456>, (2024).
- H. Blanco and A. Faaij, *Renewable Sustainable Energy Rev.*, **81**, 1049 (2018).
- M. Yue, H. Lambert, E. Pahon, R. Roche, S. Jemei, and D. Hissel, *Renewable Sustainable Energy Rev.*, **146**, 111180 (2021).
- M. Aziz, T. Oda, and T. Kashiwagi, *Energy Procedia*, **158**, 4086 (2019).
- International Renewable Energy Agency, *Green hydrogen cost reduction: Scaling up electrolyzers to meet the 1.5 °C climate goal*, p. 11 (2022).
- S. S. Kumar and H. Lim, *Energy Rep.*, **8**, 13793 (2022).
- International Energy Agency, *Global Hydrogen Review 2023*, p. 64 (2023).
- M. David, C. Ocampo-Martinez, and R. Sánchez-Peña, *J. Energy Storage*, **23**, 392 (2019).
- S. Mitsuhashi and S. Fujita, *Electrochemistry*, **85**, 28 (2017). [in Japanese]
- F. Dawood, M. Anda, and G. M. Shafullah, *Int. J. Hydrogen Energy*, **45**, 3847 (2020).
- Z. Y. Yu, Y. Duan, X. Y. Feng, X. Yu, M. R. Gao, and S. H. Yu, *Adv. Mater.*, **33**, 2007100 (2021).
- S. D. Ebbesen, S. H. Jensen, A. Hauch, and M. B. Mogensen, *Chem. Rev.*, **114**, 10697 (2014).
- M. H. Miles, G. Kissel, P. W. T. Lu, and S. Srinivasan, *J. Electrochem. Soc.*, **123**, 332 (1976).
- J. C. Ganley, *Int. J. Hydrogen Energy*, **34**, 3604 (2009).
- J. Fischer, H. Hofmann, G. Luft, and H. Wendt, *AIChE J.*, **26**, 794 (1980).
- C. R. Davidson and S. Srinivasan, *J. Electrochem. Soc.*, **127**, 1060 (1980).
- C. Davidson, G. Kissel, and S. Srinivasan, *J. Electroanal. Chem. Interfacial Electrochem.*, **132**, 129 (1982).
- C. Bailleux, *Int. J. Hydrogen Energy*, **6**, 461 (1981).
- A. C. Ferreira, E. R. Gonzalez, E. A. Ticianelli, L. A. Avaca, and B. Matvienko, *J. Appl. Electrochem.*, **18**, 894 (1988).
- Y. Ogata, H. Hori, M. Yasuda, and F. Hine, *J. Electrochem. Soc.*, **135**, 76 (1988).
- H. Wendt and V. Pizak, *Electrochim. Acta*, **28**, 27 (1983).
- R. D. Walker Jr., *A Study of Gas Solubilities and Transport Properties in Fuel Cell Electrolytes*, Research Grant NGR 10-005-022, Third Semi-Annual Report, National Aeronautics and Space Administration, Washington, D. C., p. 12 (1967).
- J. Divisek, J. Mergel, and H. F. Niessen, *Int. J. Hydrogen Energy*, **5**, 151 (1980).
- J. Divisek, J. Mergel, and H. Schmitz, *Int. J. Hydrogen Energy*, **7**, 695 (1982).
- K. Kawaguchi, K. Goto, A. Konno, and T. Nohira, *J. Electrochem. Soc.*, **170**, 084507 (2023).
- W. M. Vogel, K. J. Routsis, V. J. Kehrer, D. A. Landsman, and J. G. Tschinkel, *J. Chem. Eng. Data*, **12**, 465 (1967).
- K. Maeda, K. Yasuda, T. Nohira, R. Hagiwara, and T. Homma, *J. Electrochem. Soc.*, **162**, D444 (2015).
- M. J. Vasile and C. G. Enke, *J. Electrochem. Soc.*, **112**, 865 (1965).
- F. D. Manchester, A. San-Martin, and J. M. Pitre, *J. Phase Equilibria*, **15**, 62 (1994).
- S. M. Portnova and L. S. Itkina, *Zh. Org. Khim.*, **14**, 2187 (1969). [in Russian]
- G. J. Janz and R. Tomkins, *Physical Properties Data Compilation Relevant to Energy Storage: IV. Molten Salts: Data on Additional Single and Multi-Component Salt Systems*, National Institute of Standards and Technology, Gaithersburg, MD, p. 461 (1981).
- M. Santos, E. Silva, R. Andrade, Jr., and J. Dias, *Electrochim. Acta*, **37**, 29 (1992).
- N. Mahmood, Y. Yao, J.-W. Zhang, L. Pan, X. Zhang, and J.-J. Zou, *Adv. Sci. (Weinh.)*, **5**, 1700464 (2018).
- V. Vij, S. Sultan, A. Harzandi, A. Meena, J. Tiwari, W. Lee, T. Yoon, and K. Kim, *ACS Catal.*, **7**, 1796 (2017).
- A. Raveendran, M. Chandran, and R. Dhanuraman, *RSC Adv.*, **13**, 3843 (2023).
- S. Fletcher, *J. Solid State Electrochem.*, **13**, 537 (2009).
- K. Kinoshita, *Electrochemical Oxygen Technology*, John Wiley & Sons, Inc. (1992).
- A. C. C. Tseung and S. Jasem, *Electrochim. Acta*, **22**, 31 (1977).
- J. M. Gras and M. Pernot, *Proceedings of the Symposium on Electrode Materials and Processes for Energy Conversion and Storage*, Vol. 77-6, The Electrochemical Society Inc., Pennington, NJ, p. 425 (1977).
- P. W. T. Lu and S. Srinivasan, *J. Electrochem. Soc.*, **125**, 1416 (1978); *Proceedings of the Symposium on Electrode Materials and Processes for Energy Conversion and Storage* (Eds. J. D. E. McIntyre, S. Srinivasan, and F. G. Will), Vol. 77-6, The Electrochemical Society Inc., Pennington, NJ, p. 396 (1977).
- D. A. Corrigan, *J. Electrochem. Soc.*, **134**, 377 (1987).
- I. A. Raj, D. C. Trivdei, and V. K. Venkatesan, *Bull. Electrochem.*, **4**, 55 (1988).
- F. Song, L. Bai, A. Moysiadou, S. Lee, C. Hu, L. Liardet, and X. Hu, *J. Am. Chem. Soc.*, **140**, 7748 (2018).
- M. Plevová, J. Hnát, and K. Bouzek, *J. Power Sources*, **507**, 230072 (2021).